

Impact of iron precursors on the properties and activities of carbon-supported Fe-N oxygen reduction catalysts

Shou-Heng Liu · Jyun-Ren Wu · Feng-Sheng Zheng · Jia-Ming Guo

Received: 11 July 2014 / Revised: 13 January 2015 / Accepted: 14 January 2015 / Published online: 27 January 2015
© Springer-Verlag Berlin Heidelberg 2015

Abstract Two iron precursors (iron(III) chloride and iron(II) ammonium sulfate) with a nitrogen-containing compound (ethylenediamine) were pyrolyzed on commercially available carbon blacks (Vulcan XC-72) under a nitrogen flow in this study. The properties of the resultant nonnoble electrocatalysts (Fe(Z)N/C-2 and Fe(Z)N/C-8) effected by using different iron precursors during the synthetic process were investigated by X-ray-based spectroscopies including X-ray diffraction (XRD), X-ray photoelectron spectroscopy (XPS), and X-ray absorption spectroscopy (XAS). The electrocatalytic performance toward oxygen reduction reaction (ORR) of these electrocatalysts was also comparatively studied by rotating disk electrode and chronoamperometric techniques. The obtained results indicate that iron precursors play an essential role on the chemical microstructure, elemental states, and ORR performance of electrocatalysts. The electrocatalysts (Fe(III)N/C-8) prepared by using iron(III) chloride as starting precursors exhibit better electrochemical ORR activity and durability among all the synthesized catalysts. As evidenced by XPS and XAS studies, we conclude that this may be due to the formation of active FeN_x sites, more surface Fe/C and N/C atomic ratios, and the coexistence of pyridinic-N and graphitic-N species in the Fe(III)N/C-8 electrocatalyst.

Introduction

Direct methanol fuel cells (DMFCs) and proton-exchange membrane fuel cells (PEMFCs) as clean and high efficient

power sources have been attracting great attention for transportable and stationary applications due to their high power density, low operating temperature, and low environmental pollution. Nonetheless, the large-scale commercialization of fuel cells is limited by using expensive Pt-based catalysts as cathodic oxygen reduction reaction (ORR) [1–3]. Therefore, extensive studies [4–6] have been made on exploring new catalysts with low cost, high efficiency, and stability. In the last few decades, a variety of nonnoble metal ORR catalysts such as transition metal macrocyclic compounds [7], chalcogenides [8], conducting polymers [9], nitrogen-containing catalysts [10], and so forth have been investigated. Meanwhile, heat-treating transition metal-based nitrogen-containing complexes such as bipyridine, dibenzotetraazaannulenes, phthalocyanines, porphyrins, phenanthroline, polypyrrole, and tripyridyl triazine, etc. [11–19] has been the most promising ORR catalysts. However, the catalytic ORR performance of the abovementioned nonnoble electrocatalysts is still inferior compared to those of the Pt-based catalysts until now. Thus, the development of cost-effective method to obtain an active and durable nonnoble electrocatalysts is urgent in order to accomplish the practical and industrial implementations of DMFCs/PEMFCs.

In our previous work [20], a facile method was reported to synthesize a variety of carbon-incorporated FeN_x (FeN_xC_y) species on carbon blacks. It is noteworthy that we use a cheap and simple nitrogen-rich compound (pentaethylenehexamine) as a starting material to replace expensive heterocyclic nitrogen compounds (for instance, porphyrins and phthalocyanines) upon synthesizing carbon-incorporated FeN_x catalysts which may have potentially and effectively active sites for uses in cost-effective fuel cells. In the present study, various FeN_x electrocatalysts were synthesized by carbonizing a common nitrogen-containing compound (ethylenediamine) and two different iron precursors (iron(III) chloride and iron(II) ammonium sulfate) on carbon blacks. Consequently, a series

S.-H. Liu (✉) · J.-R. Wu · F.-S. Zheng · J.-M. Guo
Department of Chemical and Materials Engineering, National
Kaohsiung University of Applied Sciences, Kaohsiung 80778,
Taiwan
e-mail: shliu@kuas.edu.tw

of Fe(Z)N/C-2 and Fe(Z)N/C-8 (where Z=III and II represent different iron precursors) was obtained and microstructural properties as well as ORR performance have been investigated in order to explore the influence of iron precursors upon the synthetic process. In terms of catalysts' properties, X-ray-based spectroscopies including X-ray diffraction (XRD), X-ray photoelectron spectroscopy (XPS), and X-ray absorption spectroscopy (XAS) were conducted. By using XAS studies, the chemical structures of active sites and alloyed extents of target metals (PtM [21–25] and PtRu bifunctional [26, 27] electrocatalysts) have been examined thoroughly during the electrochemical processes. For studying electrocatalytic ORR performance, the linear scanning voltammetry (LSV), rotating disk electrode (RDE), and chronoamperometric techniques were employed to compare the results.

Experimental

Catalysts preparation

In a typical run, weighted amounts of FeCl₃ (Acros) or (NH₄)₂Fe(SO₄)₂·6H₂O (Acros) were dissolved in ethanol solution. To prepare the FeN_x complex solution, nitrogen-containing precursors (ethylenediamine (EDA, Acros)) were added as chelated compounds into the above solutions, followed by the introduction of carbon blacks (Vulcan XC-72, Cabot Corp.) under stirring for 48 h. Then, the solvents were removed by using a vacuum oven at 363 K. Finally, the obtained powders were pyrolyzed with a heating rate of 5 K min⁻¹ to the temperature of 1073 K in a nitrogen atmosphere and maintained at the same carbonized temperature for 2 h. The resultant samples were denoted as Fe(Z)N/C-2 and Fe(Z)N/C-8 (where Z=III and II represent the use of Fe(III)Cl₃ and (NH₄)₂Fe(II)(SO₄)₂·6H₂O, respectively, as iron precursors).

Characterizations

To obtain the bulk amounts of nitrogen in the Fe(Z)N/C-2 and Fe(Z)N/C-8 samples, elemental analyses (EA) were conducted with a CHN elemental analyzer (Heraeus varioIII). The bulk contents of iron in the samples were obtained by using an atomic absorption spectroscopy (AAS, ICE-3300). The crystallographic structures of samples were attained by using an XRD (X'Pert PRO diffractometer) under a CuK α radiation source ($\lambda=0.1541$ nm). The surface chemical environments of samples were determined by using XPS (Kratos Axis Ultra DLD) under a monochromatic Al-K α radiation (1486.6 eV). Nitrogen adsorption isotherms were measured at 77 K on a Micromeritics ASAP 2020 analyzer. The Fe K-edge (7112 eV) XAS was obtained in a transmission mode under room temperature at the Wiggler 17C beamline facility of the

National Synchrotron Radiation Research Center (NSRRC) in Taiwan. The energy resolution ($\Delta E/E$), estimated from the rocking curves of the double-crystal Si (111) monochromator, was ca. 2×10^{-4} . The intensity of the incident beam intensity (I_0) was measured by the ion chambers filled with a mixture of nitrogen and helium gases. Additionally, argon and nitrogen gases were mixed in an ion chamber to determine the transmitted beam intensity (I_t). In terms of XAS data analysis, a standard procedure including energy calibration, pre-edge and post-edge background subtraction, normalization with respect to edge height, and Fourier transformation was performed. In order to isolate the X-ray absorption fine structure (EXAFS) contributions from different coordination shells, the k^3 -weighted $\chi(k)$ spectra in the k -space range of 3.5–12.0 Å⁻¹ were Fourier-transformed (FT) to the r -space. In the present study, all the XAS data analysis was performed by using the ATHENA and ARTEMIS software [28].

Electrochemical testing

A conventional three-electrode cell was constructed to measure the electrocatalytic performance of Fe(Z)N/C-2 and Fe(Z)N/C-8 catalysts. An Ag/AgCl (saturated KCl) reference electrode and a Pt wire counter electrode were used for the half-cell system. Catalyst inks were prepared by dispersing ca. 5 mg of sample uniformly in 2.5 mL deionized water via the ultrasonic treatment. For the preparation of the working electrode, ca. 20 μ L of the above ink was deposited onto the polished glassy carbon (GC, area=0.1962 cm²) electrode, followed by drying in air at 333 K for 1 h. At last, ca. 20 μ L of 5 % Nafion[®] (DuPont) solution was applied on the catalyst-coated GC electrode to form a thin film. To clean and activate the surface of working electrode, the cyclic voltammogram (CV) was conducted by scanning the potentials between -0.2 and 1.0 V for 10 cycles in a 0.5-M H₂SO₄ solution under high-purity N₂ (99.9 %). The ORR catalytic activities of the electrocatalysts were evaluated via a LSV technique by scanning from 0.8 to -0.1 V with the scan rate of 5 mV s⁻¹ in oxygen-saturated 0.5 M H₂SO₄ electrolyte. All current-voltage (I - V) curves were measured by a potentiostat (CHI Instruments, 727D) with an RDE system (Pine Instrument, AFMSRCE) that was used to handle the rotating speed during the electrochemical tests. In addition, the rotating ring disk electrode (RRDE) was employed to measure the H₂O₂ yield by using the same electrochemical analyzer.

Results and discussion

To study the influence of iron precursors on the properties of synthesized samples, a variety of X-ray-based spectroscopic analyses were performed. Figure 1 shows the XRD patterns of

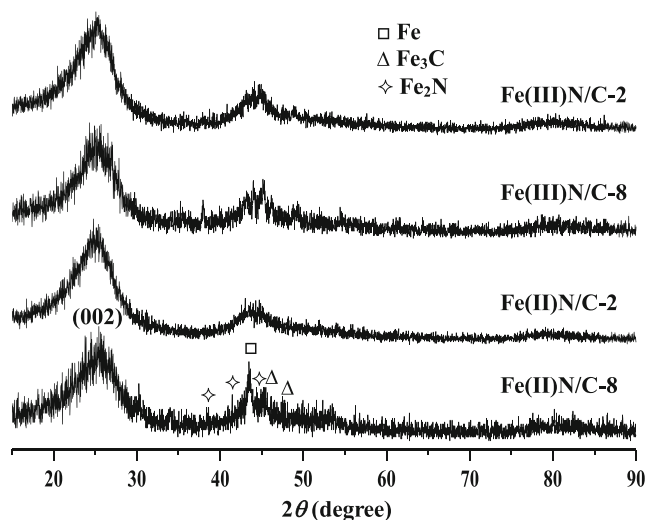


Fig. 1 XRD patterns of various Fe(Z)N/C-2 and Fe(Z)N/C-8 catalysts

Fe(Z)N/C-2 and Fe(Z)N/C-8 samples. The symbols of the square, triangle, and star in Fig. 1 represent the characteristic diffraction peaks of metallic α -Fe (JCPDS, No. 87-0722), Fe_3C (JCPDS, No. 89-2867), and Fe_2N (JCPDS, No. 89-3939), respectively. The diffraction peaks at ca. 26° observed for the samples are attributed to the (002) plane of graphitic carbon. Obviously, no noticeable diffraction peaks of Fe species were found for Fe(III)N/C-2 and Fe(II)N/C-2 samples. This is possibly because of their low contents (ca. 2 wt%) or amorphous states of Fe species. As the amount of Fe loading increased to 8 wt%, one diffraction peak at ca. 43.7° was observed for Fe(II)N/C-8 samples, suggesting the possible formation of the crystalline planes of metallic Fe. By contrast, less apparent feature of metallic Fe was found in the Fe(III)N/C-8. It can be seen that a mixture of Fe_3C , Fe_2N , and metallic Fe phases may coexist in the Fe(III)N/C-8 and Fe(II)N/C-8 samples by judging from XRD patterns. Nevertheless, it is noteworthy that chemical structures of Fe are hardly identified because the peak positions of metallic Fe, Fe_3C , and Fe_2N are rather overlaid in the XRD patterns. In addition, it is likely that some Fe species are unable to be observed by means of XRD

due to their presence of amorphous phases. Therefore, to further investigate the information including the chemical environment of Fe, the coordination geometry, and the bonding of its local environment around the Fe atoms, additional X-ray based spectroscopies (XPS and XAS) were carried out.

XPS analysis was employed to reveal the surface chemical compositions of Fe(Z)N/C-2 and Fe(Z)N/C-8 samples. From the full-range XPS survey (not shown), all the samples mostly contain four species including carbon (C 1s, 279–293 eV), nitrogen (N 1s, 395–407 eV), oxygen (O 1s, 525–537 eV), and iron (Fe 2p, 700–740 eV). As a result, their corresponding surface atomic contents (at.%) are summarized and compared in Table 1. As we can see, Fe(III)N/C-2 and Fe(III)N/C-8 samples synthesized using FeCl_3 as iron precursors possess higher surface atomic nitrogen contents (1.0 and 1.5 at.%, respectively) than the bulk nitrogen contents (0.9 and 0.8 %, respectively). Nonetheless, the Fe(II)N/C-2 and Fe(II)N/C-8 samples have lower surface atomic (0.7 and 0.6 at.%, respectively) and bulk nitrogen contents (0.7 and 0.5 %, respectively) when compared to Fe(III)N/C-2 and Fe(III)N/C-8 samples. These results imply the preferential formation of nitrogen atoms on the sample surface upon using FeCl_3 precursors in the synthesis process. As reported earlier [15], the better ORR activity can be achieved as the higher amounts of nitrogen were doped onto the catalysts surface. To further realize the structural states of these nitrogen species on the surfaces of Fe(Z)N/C-2 and Fe(Z)N/C-8 samples, high-resolution XPS N 1s spectra are attained and shown in Fig. 2. Three Lorentzian-Gaussian multi-peaks at ca. 398.5 (pyridinic-N), 400.9 (graphitic-N), and 401.5 (pyridinic-N-H) were obtained by deconvoluting the broad peaks of all samples. The first peak at ca. 398.5 eV (pyridinic-N) [29] represents nitrogen atoms doped at the edges of the graphitic carbon layer. The second feature at ca. 400.9 eV (graphitic-N/quaternary-N) [29] is defined as nitrogen atoms doped inside the graphitic carbon plane. In the previous report [30], pyridinic-N and graphitic-N are the dominant species influencing the ORR activities, whereas the third peak at ca. 401.5 eV may be ascribed to pyridinic-N-H which is reported to be ORR inactive species

Table 1 Physical properties of various Fe(Z)N/C-2 and Fe(Z)N/C-8 catalysts

Sample	N ^a (%)	Fe ^b (%)	C ^c (at.%)	N ^c (at.%)	O ^c (at.%)	Fe ^c (at.%)	N/C ^d	Fe/C ^d	S_{BET}^e ($\text{m}^2 \text{g}^{-1}$)
Fe(III)N/C-2	0.9	3.4	87.0	1.0	11.0	1.0	0.011	0.011	296
Fe(III)N/C-8	0.8	8.0	80.8	1.5	16.3	1.4	0.019	0.017	174
Fe(II)N/C-2	0.7	1.9	85.3	0.7	13.2	0.8	0.008	0.009	141
Fe(II)N/C-8	0.5	7.6	88.5	0.6	9.7	1.2	0.007	0.013	120

^a Determined by EA

^b Fe content (wt%) analyzed by AAS

^c Obtained from XPS analysis

^d Atomic ratio between N and C calculated from the table

^e Brunauer-Emmett-Teller (BET) surface areas

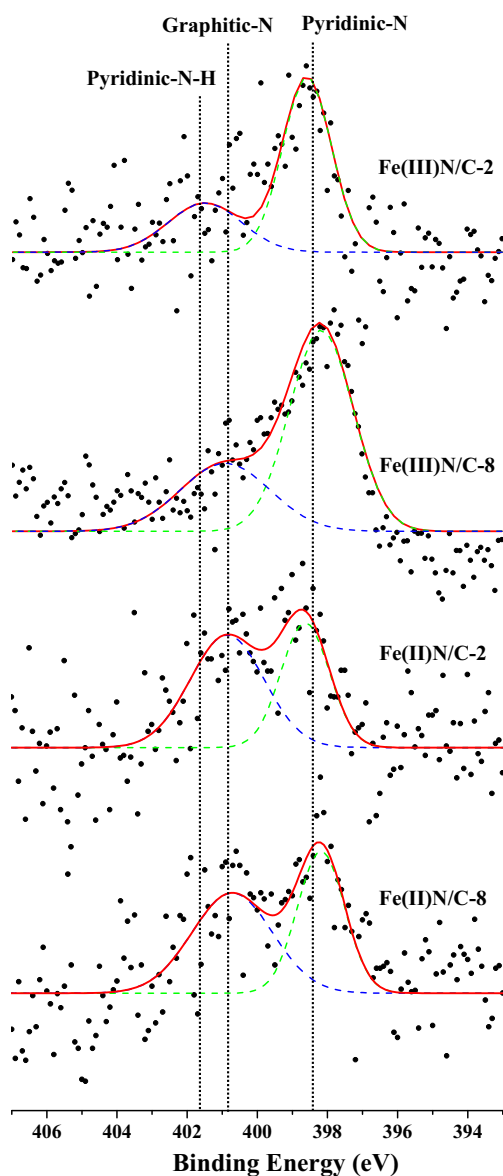


Fig. 2 XPS spectra of various Fe(Z)N/C-2 and Fe(Z)N/C-8 catalysts at the N 1s region

[31]. To quantitatively obtain the relative fractions of the nitrogen species on the surfaces of Fe(Z)N/C-2 and Fe(Z)N/C-8 samples, further spectra analyses by Lorentzian-Gaussian deconvolution were conducted and listed in Table 2. It can be observed that Fe(III)N/C-2 samples exhibit two major nitrogen-doping types of pyridinic-N (71 %) and pyridinic-N-H (29 %). Interestingly, pyridinic-N-H may be converted to graphitic-N in the Fe(III)N/C-8 samples while the content of Fe is increased to 8 wt%. In addition, while the Fe precursors were changed to $(\text{NH}_4)_2\text{Fe}(\text{SO}_4)_2 \cdot 6\text{H}_2\text{O}$ during the synthesis process, pyridinic-N and graphitic-N are the main nitrogen-doping types in the Fe(II)N/C-2 and Fe(II)N/C-8 samples. In the latest studies [32–34], graphitic-N is considered to be the superior sites of nitrogen-doped carbons during ORR. On the contrary, pyridinic-N is responsible for

Table 2 Surface atomic concentrations of different types of N species in various Fe(Z)N/C-2 and Fe(Z)N/C-8 catalysts obtained from XPS results

Sample	Assignment	Concentration
Fe(III)N/C-2	Pyridinic-N	0.71
	Pyridinic-N-H	0.29
Fe(III)N/C-8	Pyridinic-N	0.68
	Graphitic-N	0.32
Fe(II)N/C-2	Pyridinic-N	0.42
	Graphitic-N	0.58
Fe(II)N/C-8	Pyridinic-N	0.45
	Graphitic-N	0.55

significant enhancement of the ORR activity [35] according to previous reports. Additionally, the pyridinic-N is not able to assist direct four-electron pathways for ORR without the help of graphitic-N [35, 36]. It seems that the role of actual electrocatalytic active sites is still contentious. However, the co-existence of pyridinic-N and graphitic-N species in this work is recognized as the most active sites for catalyzing ORR. In particular for Fe(III)N/C-8 samples, the higher concentrations of pyridinic-N (68 %) and the assistance of graphitic-N (32 %) as well as an increase in the surface nitrogen content (1.5 at.%) should be responsible for the observed enhancement of ORR activity (discussed below).

Table 1 also shows the surface iron contents of Fe(Z)N/C-2 and Fe(Z)N/C-8 samples. It can be seen that the contents of Fe are only 0.8–1.4 at.%, indicating their rather low loadings on the surface of samples. Among them, Fe(III)N/C-8 samples possess the highest surface iron content (1.4 at.%) and atomic Fe/C ratio (0.017), suggesting that the Fe atoms present more on the surface of Fe(III)N/C-8 than those of other samples. In addition, the higher specific surface areas (see Table 1) can be found in the Fe(III)N/C-2 and Fe(III)N/C-8 catalysts than those in the Fe(II)N/C-2 and Fe(II)N/C-8, suggesting that iron precursors significantly affect the surface areas of micropores

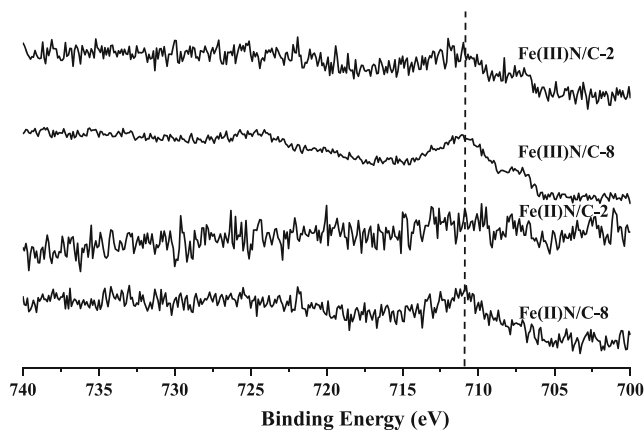


Fig. 3 XPS spectra of Fe(Z)N/C-2 and Fe(Z)N/C-8 catalysts at the Fe 2p region

during the synthesis process. As displayed in Fig. 3, moreover, the high-resolution Fe 2p spectra show that the binding energies of Fe(Z)N/C-2 and Fe(Z)N/C-8 samples in the Fe 2p_{3/2} region are all located at ca. 711.4 eV, indicating that the presence of oxidative surface Fe(III) state is based on the peak positions of the Fe (III) 2p_{3/2} binding energy (710.8–711.8 eV) and Fe(II) 2p_{3/2} binding energy (707.1–708.7 eV) [37]. Interestingly, no evident peak was observed at ca. 706.7 eV, implying the nonexistence of the iron nitride species [38] on the surface of Fe(Z)N/C-2 and Fe(Z)N/C-8 samples.

To more realize the nature of iron active sites in the Fe(Z)N/C-2 and Fe(Z)N/C-8 samples during ORR, further XAS analyses were performed. Figure 4a shows the normalized K-edge EXAFS spectra of Fe(Z)N/C-2, Fe(Z)N/C-8 samples, and

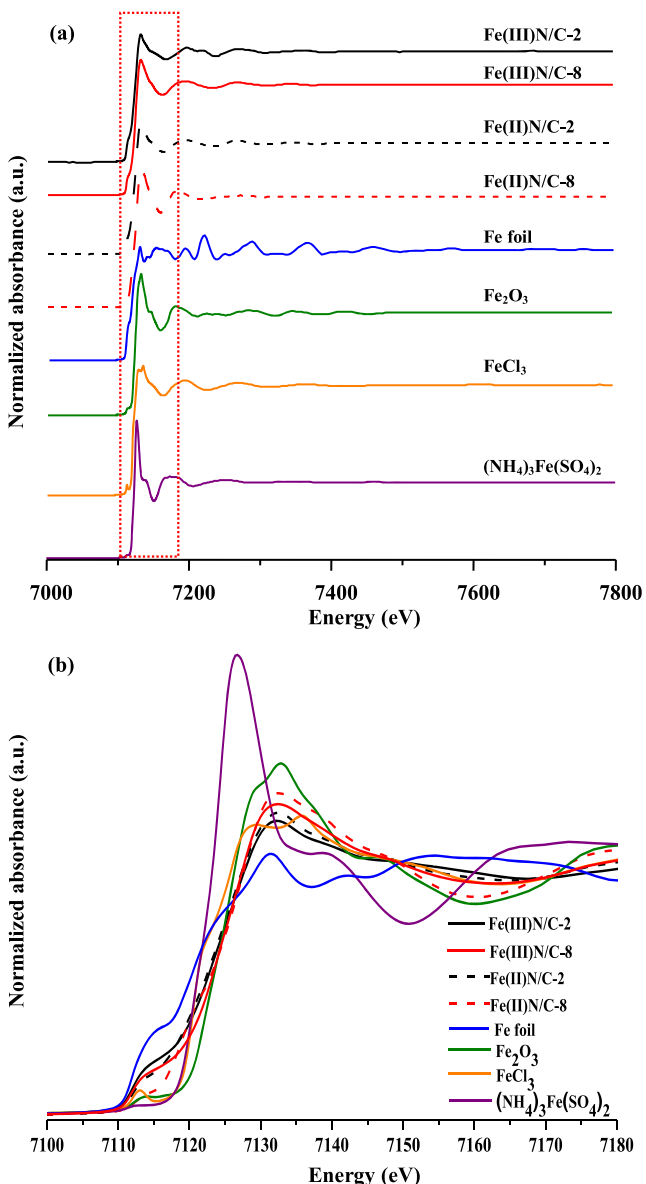


Fig. 4 a Fe K-edge XANES spectra and b their corresponding magnification spectra of Fe(Z)N/C-2 and Fe(Z)N/C-8 catalysts and Fe standard compounds

model compounds (Fe foil, Fe₂O₃, FeCl₃, and (NH₄)₃Fe(SO₄)₂). Obviously, it can be seen that the shapes of the Fe(Z)N/C-2 and Fe(Z)N/C-8 samples in the XANES regions are diverse as compared to those of the model compounds. This result shows that the iron precursors (FeCl₃ and (NH₄)₃Fe(SO₄)₂) have been converted to different forms of iron upon chelating and heat-treated carbonization processes. To recognize the corresponding positions of the edge caused by the excitation of a core electron to quasi-bound states [39] which are related to the valence of the iron atom, the high-resolution Fe K-edge XANES is shown in Fig. 4b. The curves of Fe(Z)N/C-2 and Fe(Z)N/C-8 samples in the XANES regions are located between those of Fe foil and Fe₂O₃, suggesting the existence of the oxidative valence of iron. In addition, the white line intensities (the magnitude of absorption hump at ca. 7128 eV) of samples are between those from Fe foil and Fe₂O₃, suggesting that iron species are present as oxidative states which are consistent with the above results. Additionally, the edges of Fe(III)N/C-2 and Fe(III)N/C-8 catalysts shift toward higher values at the absorption energy edges, suggesting their existence of large valences. Fourier transformations of the *k*³-weighted EXAFS functions observed for Fe(Z)N/C-2 and Fe(Z)N/C-8 samples and model compounds are shown in Fig. 5. It can be seen that the radial distance distributions of

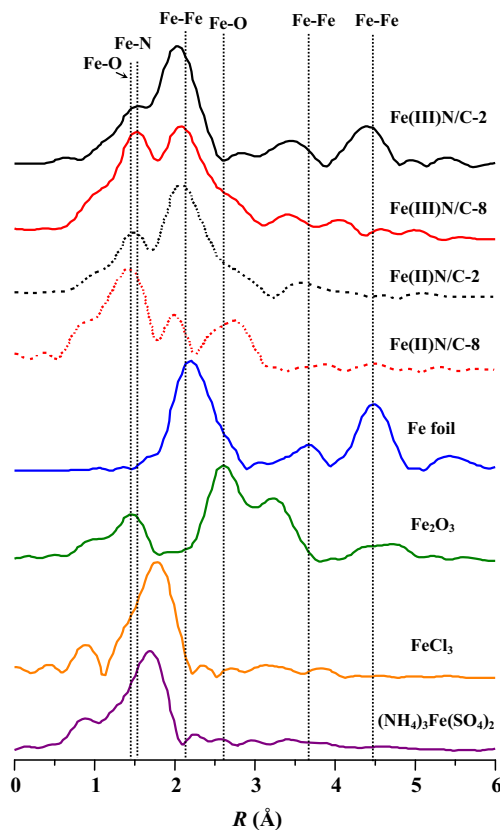


Fig. 5 Radial distribution functions of Fourier-transformed *k*³-weighted $\chi(k)$ Fe K-edge EXAFS spectrum for Fe(Z)N/C-2 and Fe(Z)N/C-8 catalysts and Fe standard compounds

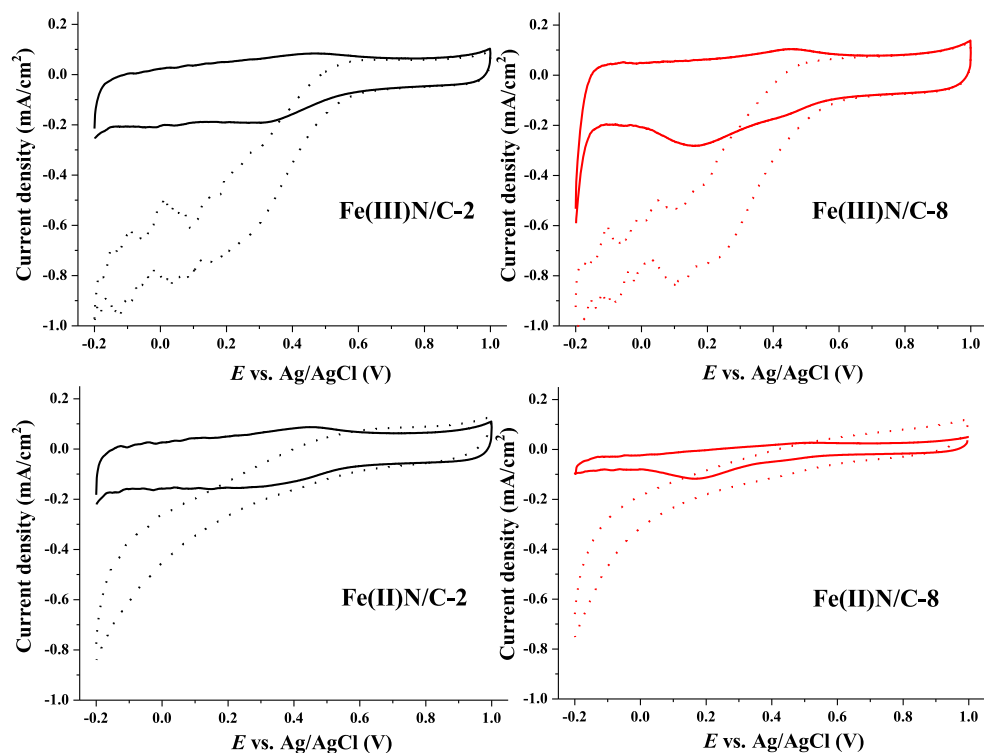
Fe(Z)N/C-2 and Fe(Z)N/C-8 samples are different from those of model compounds, implying that these samples may be formed in the diverse local structures. The first peaks observed for Fe(Z)N/C-2 and Fe(Z)N/C-8 samples in the FT spectra are due to Fe-N or Fe-O bonds in the first shells. The second features are ascribed to the Fe-Fe bonds in the second coordination shells. The other peaks may be the Fe-Fe bonds in the higher coordination shells. Obviously, Fe(II)N/C-2 and Fe(II)N/C-8 samples possess mainly Fe-O bonds in the first shells, while large amounts of Fe-N bonding structure are found in the Fe(III)N/C-2 and Fe(III)N/C-8 samples. In addition, Fe(II)N/C-2 and Fe(III)N/C-2 samples have apparent Fe-Fe bonds in the second (or higher) coordination shells, implying that the aggregation of iron metals may occur. As a result, the Fe-N structure can be significantly formed in the samples synthesized from FeCl₃ precursors. Interestingly, however, the increased intensities in the second shell coordination of Fe-Fe moieties observed for Fe(II)N/C-2 and Fe(III)N/C-2 samples indicate that the sintering reactions between metallic iron species may happen during high temperature carbonization process.

As displayed in Fig. 6, CVs of the glassy carbon electrode surfaces coated by Fe(Z)N/C-2 and Fe(Z)N/C-8 catalysts measured in a N₂-purging 0.5 M H₂SO₄ solution show weak features of redox waves in the potential range of -0.2 to 1.0 V. By contrast, the cathodic currents with the potentials ranging from 0.2 to 0.7 V can be evidently observed for Fe(III)N/C-2 and Fe(III)N/C-8 in a O₂-purging 0.5 M H₂SO₄ solution,

indicating the pronounced occurrence of ORR on these catalysts. Among these electrocatalysts, Fe(III)N/C-8 catalysts possess the largest capacitance over the measured range of potentials, suggesting that it has the largest catalytic surface area. The higher capacitance values can result in the higher electrochemical surface and faster electron transfer which could lead to the surpassing of ORR activity.

The ORR performance of Fe(Z)N/C-2 and Fe(Z)N/C-8 catalysts was assessed by LSV in oxygen-saturated 0.5 M H₂SO₄ solution at room temperature. Figure 7 displays the polarization curves of these catalysts and their corresponding onset and half-wave potentials are also listed in Table 3. The Fe(III)N/C-2 electrocatalysts showed ORR activities at the onset and half-wave potentials of ca. 0.57 and 0.33 V vs. Ag/AgCl, respectively. Upon increasing the iron contents to 8 wt%, the onset and half-wave potentials were further increased to 0.61 and 0.40 V vs. Ag/AgCl. While the (NH₄)₂Fe(SO₄)₂·6H₂O was used as iron precursors in the synthesis, the ORR activities of Fe(II)N/C-2 and Fe(II)N/C-8 were found to be remarkably decreased. It is clear that the iron precursors have an essential impact on the ORR activities of Fe(Z)N/C-2 and Fe(Z)N/C-8 catalysts. The ORR onset potentials of the Fe(Z)N/C-2 and Fe(Z)N/C-8 catalysts follows the order: Fe(III)N/C-8 > Fe(III)N/C-2 > Fe(II)N/C-8 ≈ Fe(II)N/C-2. In order to further explore the ORR mechanism on the catalysts prepared from different iron precursors, the RDE technique was carried out in O₂-saturated 0.5 M H₂SO₄ solution at room temperature under different rotating rates.

Fig. 6 CV curves of Fe(Z)N/C-2 and Fe(Z)N/C-8 catalysts on a glassy carbon electrode surface measured under N₂-saturated (solid lines) and O₂-saturated (dot lines) 0.5 M H₂SO₄ solution at a scan rate of 10 mV s⁻¹



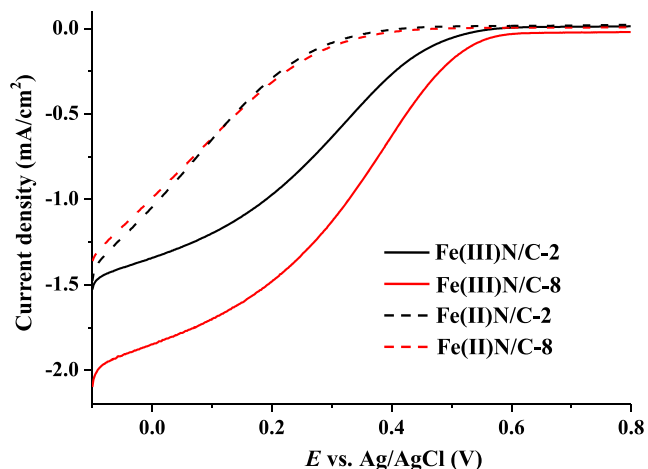


Fig. 7 Polarization curves during oxygen reduction for various Fe(Z)N/C-2 and Fe(Z)N/C-8 catalysts in O₂-saturated 0.5 M H₂SO₄ solution at room temperature

Consequently, the number of transferred electrons (n) during ORR can be attained from the slope by using the Koutecky-Levich first-order reaction equation [40]:

$$j^{-1} = j_k^{-1} + j_d^{-1}$$

where j is the measured current density, j_k is the kinetic current density for the ORR, and j_d is the diffusion-limiting current density that can be expressed by the following equations:

$$j_d = B \omega^{1/2}$$

$$B = 0.62nFC_{O_2}D_{O_2}^{2/3}\nu^{-1/6}$$

where B represents the Levich slope, ω denotes the rotating angular frequency, n is the number of the exchange electrons during the ORR process, F is Faraday constant (96,487 C mol⁻¹), C_{O_2} and D_{O_2} , respectively, represent the concentration and diffusion coefficient of oxygen dissolved in the electrolyte, and ν is the kinematic viscosity of the electrolyte (0.01 cm² s⁻¹). The RDE voltammograms of various Fe(Z)N/C-2 and Fe(Z)N/C-8 electrocatalysts in O₂-saturated 0.5 M H₂SO₄ solution at room temperature under different

Table 3 Kinetic parameters of various Fe(Z)N/C-2 and Fe(Z)N/C-8 electrocatalysts during ORR

Sample	E_{onset}^a (V)	$E_{\text{half-wave}}^b$ (V)	n
Fe(III)N/C-2	0.57	0.33	2.2
Fe(III)N/C-8	0.61	0.40	3.0
Fe(II)N/C-2	0.42	0.11	1.4
Fe(II)N/C-8	0.42	0.11	2.4

^a Onset potential vs. Ag/AgCl

^b Half-wave potential vs. Ag/AgCl

rotation rates are displayed in Fig. 8 and their corresponding Koutecky-Levich plots at different potentials are shown in Fig. 9. As shown in Table 3, the n values of the catalysts prepared from (NH₄)₂Fe(SO₄)₂·6H₂O precursors are obviously lower than 4, indicating the catalyzed ORR with both two-electron-transferred reduction and four-electron-transferred reduction, while the former is dominant. On the other hand, the Fe(III)N/C-8 catalysts proceed more four-electron-transferred reaction as compared to the Fe(II)N/C-2 and Fe(II)N/C-8 catalysts. Thus, the iron precursors have a critical influence on ORR mechanism which is in accordance with the order of catalytic activities discussed above.

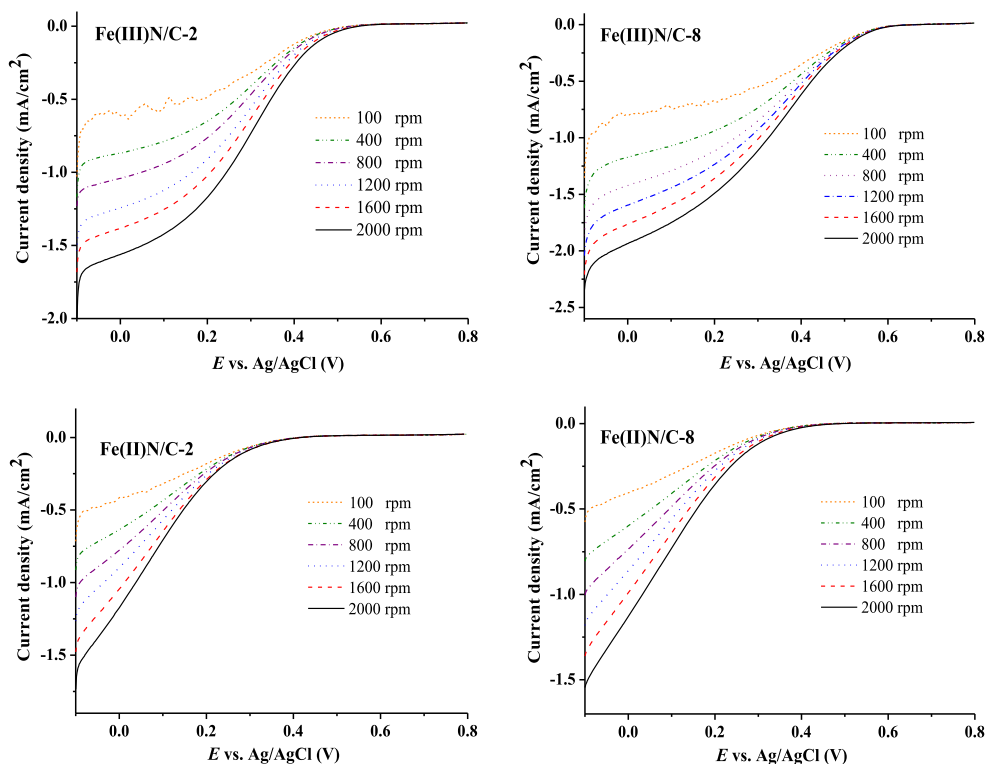
The RRDE voltammetry curves which can be used to evaluate the generated amount of hydrogen peroxide during the ORR process of Fe(Z)N/C-2 and Fe(Z)N/C-8 electrocatalysts are also shown in Fig. 10a. The yields of hydrogen peroxide were determined by using the equation [41]:

$$\%H_2O_2 = \frac{2I_r}{N \times I_d + I_r} \times 100\%$$

where I_d (see in Fig. 7), I_r (see in Fig. 10a), and N (0.24 in this work) are the disk current, ring current, and collection efficiency, respectively. As a result, the fractional yields of hydrogen peroxide for the synthesized electrocatalysts were obtained and illustrated in Fig. 10b. It can be seen that Fe(III)N/C-2 and Fe(III)N/C-8 electrocatalysts have superior ORR activity and generated a less amount of hydrogen peroxide during the reaction as compared to Fe(II)N/C-2 and Fe(II)N/C-8.

More importantly, tolerance to methanol crossover and electrocatalytic durability at the cathode have been two of the vital requirements for practical applications of fuel cells [42–44]. To further investigate the methanol-tolerant behaviors of the synthesized electrocatalysts, LSV tests were also carried out to realize the effect of various concentrations of methanol (0.5–2.0 M) on electrocatalytic ORR activities of Fe(III)N/C-8 catalysts. As shown in Fig. 11, it can be seen that the overpotential of Fe(III)N/C-8 electrocatalysts is intact upon the presence of 0.5 M methanol. A slight decrease with a current density loss of ca. 10 % measured at 0.5 V vs. Ag/AgCl was observed even in the existence of 2.0 M methanol while compared to ORR in pure H₂SO₄ solution. The significant resistance to methanol during ORR on the Fe(III)N/C-8 catalysts is due to the weak competition reaction between oxygen reduction and methanol oxidation. In addition, the stability of Fe(Z)N/C-2 and Fe(Z)N/C-8 catalysts also can be evaluated by investigating the current loss after prolonged operation (ca. 13.9 h) at a constant voltage of 0.4 V vs. Ag/AgCl in a 0.5-M H₂SO₄ electrolyte saturated with O₂ at a rotating rate of 1600 rpm. As shown in Fig. 12, the order of current-time ($i-t$) chronoamperometric response of Fe(III)N/C-2 > Fe(III)N/C-8 > Fe(II)N/C-2 > Fe(II)N/C-8 was observed

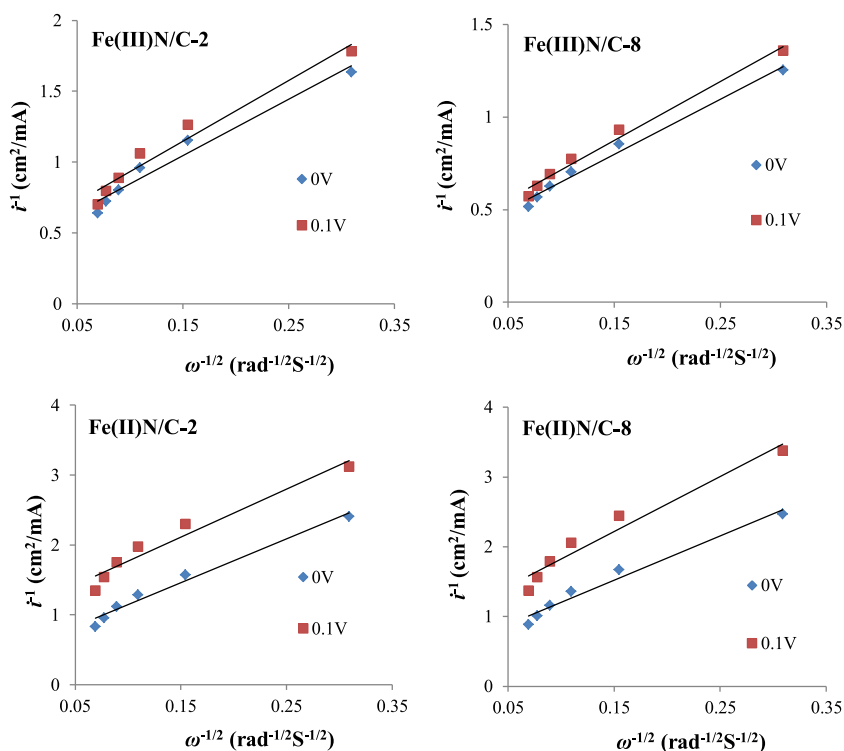
Fig. 8 RDE voltammograms for the Fe(Z)N/C-2 and Fe(Z)N/C-8 in O₂-saturated 0.5 M H₂SO₄ with various rotation rates



after 13.9 h operation. These results of durability testing indicate that ORR performance of synthesized catalysts using FeCl₃ as iron precursors is surpassing than those using

(NH₄)₂Fe(SO₄)₂·6H₂O as iron precursors. Based on the combined results from X-ray-based spectroscopies (XRD, XPS, and XAS), the better ORR performance (both activity and

Fig. 9 Koutecky-Levich plots for the Fe(Z)N/C-2 and Fe(Z)N/C-8 electrocatalysts at different electrode potentials



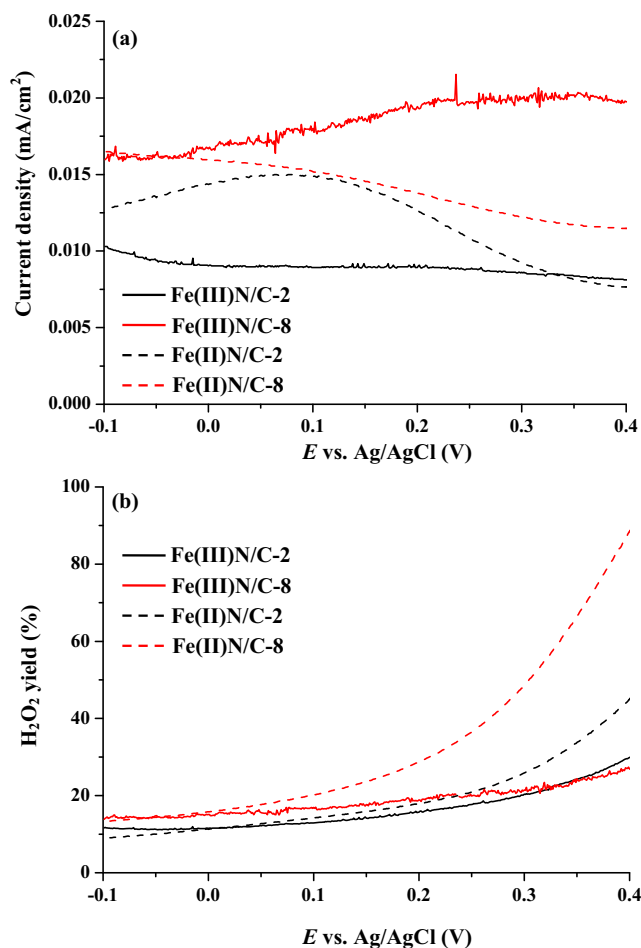


Fig. 10 **a** RRDE data of hydrogen peroxide yield and **b** fractional yield of hydrogen peroxide for Fe(Z)N/C-2 and Fe(Z)N/C-8 electrocatalysts

durability) of Fe(III)N/C-8 catalysts is possibly attributed to the more atomic ratios of surface N/C and Fe/C with the formation of FeN_x species that iron may be coordinated with pyridinic-N and graphitic-N active sites.

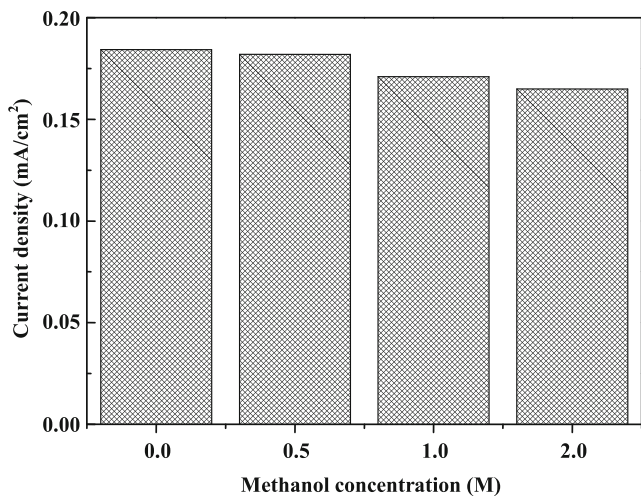


Fig. 11 Effect of methanol concentrations on ORR activities of Fe(III)N/C-8 at 0.5 V vs. Ag/AgCl in O₂-saturated 0.5 M H₂SO₄ solution

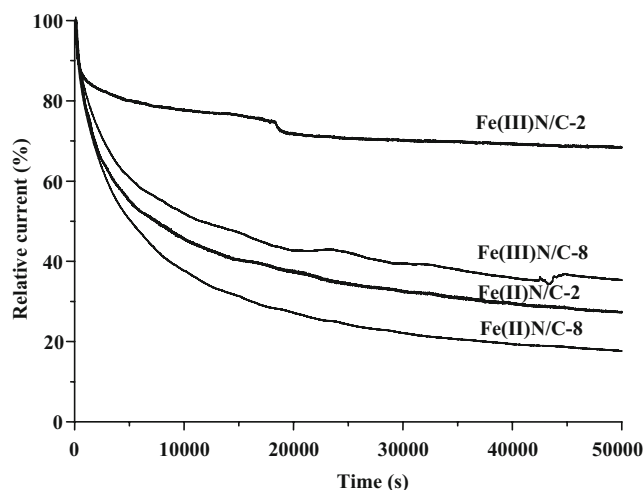


Fig. 12 Chronoamperometric analysis of Fe(Z)N/C-2 and Fe(Z)N/C-8 catalysts at 0.4 V vs. Ag/AgCl in O₂-saturated 0.5 M H₂SO₄ solution at room temperature

Conclusions

In this study, various nonnoble FeN_x electrocatalysts (Fe(Z)N/C-2 and Fe(Z)N/C-8, Z=III and II) were fabricated by heat-treating two iron precursors (Fe(III)Cl₃ and (NH₄)₂Fe(II)(SO₄)₂·6H₂O) with a simple nitrogen-containing precursor (ethylenediamine) on carbons in a nitrogen atmosphere. The influence of iron precursors on the catalysts properties and ORR performance has been comparatively examined with a series of electrochemical analysis techniques including cyclic voltammogram, rotating disk electrode, and chronoamperometric methods. In addition, the physiochemical properties of Fe(Z)N/C-2 and Fe(Z)N/C-8 catalysts were analyzed and discussed by using various X-ray-based techniques. As a result, we found that iron precursors play a critical role on the microstructures of the synthesized catalysts and their corresponding ORR activities. Among all the catalysts, those prepared with FeCl₃ precursors have the surpassing ORR performance. By employing XPS analysis, Fe(III)N/C-8 catalysts were found to have the notable increases in the atomic surface Fe/C and N/C ratios with coexistence of pyridinic-N (68 %) and graphitic-N (32 %) sites. Additionally, the FeN_x clusters, which may be the active centers for the superior ORR activity and durability, can be observed for the Fe(III)N/C-8 catalysts in the analysis of XAS. Consequently, the developed nonnoble nanocatalysts may be possible electrocatalysts for practical implementations in DMFCs and PEMFCs.

Acknowledgments Financial support of this work from the Ministry of Science and Technology of Taiwan (Contract No. NSC99-2221-E-151-044-MY2) is gratefully acknowledged.

References

1. Guterman VE, Lastovina TA, Belenov SV, Tabachkova NY, Vlasenko VG, Khodos II, Balakshina EN (2014) Pt/M/C (M = Ni, Cu, or Ag) electrocatalysts: effects of alloying components on morphology and electrochemically active surface areas. *J Solid State Electrochem* 18(5):1307–1317
2. Liu S-H, Chen S-C, Sie W-H (2011) Heat-treated platinum nanoparticles embedded in nitrogen-doped ordered mesoporous carbons: synthesis, characterization and their electrocatalytic properties toward methanol-tolerant oxygen reduction. *Int J Hydrogen Energy* 36:15060–15067
3. Sepp S, Haerk E, Valk P, Vaarmets K, Nerut J, Jaeger R, Lust E (2014) Impact of the Pt catalyst on the oxygen electroreduction reaction kinetics on various carbon supports. *J Solid State Electrochem* 18(5):1223–1229
4. Brouzougou A, Song SQ, Tsiakaras P (2012) Low and non-platinum electrocatalysts for PEMFCs: current status, challenges and prospects. *Appl Catal B Environ* 127:371–388
5. Soin N, Roy SS, Sharma S, Thundat T, McLaughlin JA (2013) Electrochemical and oxygen reduction properties of pristine and nitrogen-doped few layered graphene nanoflakes (FLGs). *J Solid State Electrochem* 17(8):2139–2149
6. Liu S-H, Zheng F-S, Wu J-R (2011) Preparation of ordered mesoporous carbons containing well-dispersed and highly alloying Pt-Co bimetallic nanoparticles toward methanol-resistant oxygen reduction reaction. *Appl Catal B Environ* 108:81–89
7. Yin W, Chen CG, Fa HB, Zhang LP (2013) Electropolymerization of CoTPP and its catalytic performance for oxygen-reduction reaction in an acid medium. *J Solid State Electrochem* 17(12):3095–3099
8. Ziegelbauer JM, Gatewood D, Gulla AF, Guinel MJF, Ernst F, Ramaker DE, Mukerjee S (2009) Fundamental investigation of oxygen reduction reaction on rhodium sulfide-based chalcogenides. *J Phys Chem C* 113:6955–6968
9. Dorjgotov A, Ok J, Jeon Y, Yoon SH, Shul YG (2013) Nitrogen-doped ordered porous carbon catalyst for oxygen reduction reaction in proton exchange membrane fuel cells. *J Solid State Electrochem* 17(10):2567–2577
10. Ganesan S, Leonard N, Barton SC (2014) Impact of transition metal on nitrogen retention and activity of iron-nitrogen-carbon oxygen reduction catalysts. *Phys Chem Chem Phys* 16(10):4576–4585
11. Bezerra CWB, Zhang L, Lee K, Liu H, Marques ALB, Marques EP, Wang HJ, Zhang JJ (2008) A review of Fe-N/C and Co-N/C catalysts for the oxygen reduction reaction. *Electrochim Acta* 53:4937–4951
12. Liu G, Li X, Ganesan P, Popov BN (2009) Development of non-precious metal oxygen-reduction catalysts for PEM fuel cells based on N-doped ordered porous carbon. *Appl Catal B Environ* 93:156–165
13. Zhang L, Lee K, Bezerra CWB, Zhang JL, Zhang JJ (2009) Fe loading of a carbon-supported Fe-N electrocatalyst and its effect on the oxygen reduction reaction. *Electrochim Acta* 54:6631–6636
14. Charreterre F, Jaouen F, Dodelet JP (2009) Iron porphyrin-based cathode catalysts for PEM fuel cells: influence of pyrolysis gas on activity and stability. *Electrochim Acta* 54:6622–6630
15. Choi JY, Hsu RS, Chen ZW (2010) Highly active porous carbon-supported nonprecious metal-N electrocatalyst for oxygen reduction reaction in PEM fuel cells. *J Phys Chem C* 114:8048–8053
16. Palaniselvam T, Aiyappa HB, Kurungot S (2012) An efficient oxygen reduction electrocatalyst from graphene by simultaneously generating pores and nitrogen doped active site. *J Mater Chem* 22:23799–23805
17. Brocato S, Serov A, Atanassov P (2013) pH dependence of catalytic activity for ORR of the non-PGM catalyst derived from heat-treated Fe-phenanthroline. *Electrochim Acta* 87:361–365
18. Liu Y, Wu YY, Lv GL, Pu T, He XQ, Cui LL (2013) Iron(II) phthalocyanine covalently functionalized graphene as a highly efficient non-precious-metal catalyst for the oxygen reduction reaction in alkaline media. *Electrochim Acta* 112:269–278
19. Yuan XX, Hu XX, Ding XL, Kong HC, Sha HD, Lin H, Wen W, Shen GX, Guo Z, Ma Z, Yang Y (2013) Effects of cobalt precursor on pyrolyzed carbon-supported cobalt-polypyrrole as electrocatalyst toward oxygen reduction reaction. *Nanoscale Res Lett* 8:478
20. Liu S-H, Wu J-R, Pan C-J, Hwang B-J (2014) Synthesis and characterization of carbon incorporated Fe-N/carbon for methanol-tolerant oxygen reduction reaction of polymer electrolyte fuel cells. *J Power Sources* 250:279–285
21. Lima FHB, de Castro JFR, Santos LGRA, Ticianelli EA (2009) Electrocatalysis of oxygen reduction on carbon-supported Pt-Co nanoparticles with low Pt content. *J Power Sources* 190:293–300
22. Malheiro AR, Perez J, Villullas HM (2010) Surface structure and electronic properties of Pt-Fe/C nanocatalysts and their relation with catalytic activity for oxygen reduction. *J Power Sources* 195:3111–3118
23. Hwang SJ, Yoo SJ, Jang S, Lim TH, Hong SA, Kim SK (2011) Ternary Pt-Fe-Co alloy electrocatalysts prepared by electrodeposition: elucidating the roles of Fe and Co in the oxygen reduction reaction. *J Phys Chem C* 115:2483–2488
24. Loukrakpam R, Luo J, He T, Chen YS, Xu ZC, Njoki PN, Wanjala BN, Fang B, Mott D, Yin J, Klar J, Powell B, Zhong CJ (2011) Nanoengineered PtCo and PtNi catalysts for oxygen reduction reaction: an assessment of the structural and electrocatalytic properties. *J Phys Chem C* 115:1682–1694
25. Ishiguro N, Saida T, Uruga T, Nagamatsu S, Sekizawa O, Nitta K, Yamamoto T, Ohkoshi S, Iwasawa Y, Yokoyama T, Tada M (2012) Operando time-resolved X-ray absorption fine structure study for surface events on a Pt₃Co/C cathode catalyst in a polymer electrolyte fuel cell during voltage-operating processes. *ACS Catal* 2:1319–1330
26. Liu S-H, Yu W-Y, Chen C-H, Lo A-Y, Hwang B-J, Chien S-H, Liu S-B (2008) Fabrication and characterization of well-dispersed and highly stable PtRu nanoparticles on carbon mesoporous material for applications in direct methanol fuel cell. *Chem Mater* 20:1622–1628
27. Goto S, Hosoi S, Arai R, Tanaka S, Umeda M, Yoshimoto M, Kudo Y (2014) Particle-size- and Ru-core-induced surface electronic states of Ru-core/Pt-shell electrocatalyst nanoparticles. *J Phys Chem C* 118:2634–2640
28. Ravel B, Newville M (2005) ATHENA, ARTEMIS, HEPHAESTUS: data analysis for X-ray absorption spectroscopy using IFEFFIT. *J Synchrotron Radiat* 12:537–541
29. Pels JR, Kapteijn F, Moulijn JA, Zhu Q, Thomas KM (1995) Evolution of nitrogen functionalities in carbonaceous materials during pyrolysis. *Carbon* 33:1641–1653
30. Oh HS, Kim H (2012) The role of transition metals in non-precious nitrogen-modified carbon-based electrocatalysts for oxygen reduction reaction. *J Power Sources* 212:220–225
31. Liu G, Li XG, Lee JW, Popov BN (2011) A review of the development of nitrogen-modified carbon-based catalysts for oxygen reduction at USC. *Catal Sci Technol* 1:207–217
32. Kim H, Lee K, Woo SI, Jung YS (2011) On the mechanism of enhanced oxygen reduction reaction in nitrogen-doped graphene nanoribbons. *Phys Chem Chem Phys* 13:17505–17510
33. Zhang J, He DP, Su H, Chen X, Pan M, Mu SC (2014) Porous polyaniline-derived FeN_x/C catalysts with high activity and stability towards oxygen reduction reaction using ferric chloride both as an oxidant and iron source. *J Mater Chem A* 2:1242–1246
34. Sevilla M, Yu LH, Feller TP, Fuertes AB, Titirici M (2013) Polypyrrole-derived mesoporous nitrogen-doped carbons with intrinsic catalytic activity in the oxygen reduction reaction. *RSC Adv* 3:9904–9910
35. Luo Z, Lim S, Tian Z, Shang J, Lai L, MacDonald B, Fu C, Shen ZX, Yu T, Lin JY (2011) Pyridinic N doped graphene: synthesis,

- electronic structure, and electrocatalytic property. *J Mater Chem* 21: 8038–8044
36. Unni SM, Devulapally S, Karjule N, Kurungot S (2012) Graphene enriched with pyrrolic coordination of the doped nitrogen as an efficient metal-free electrocatalyst for oxygen reduction. *J Mater Chem* 22(44):23506–23513
 37. Choudhury T, Saied SO, Sullivan JL, Abbot AM (1989) Reduction of oxides of iron, cobalt, titanium and niobium by low-energy ion bombardment. *J Phys D Appl Phys* 22:1185–1195
 38. Biwer BM, Bernasek SL (1986) Electron spectroscopic study of the iron surface and its interaction with oxygen and nitrogen. *J Electron Spectrosc Relat Phenom* 40:339–351
 39. Iwasawa Y (1996) X-ray absorption fine structure for catalyst and surfaces. World Scientific, Singapore
 40. Liu S-H, Wu M-T, Lai Y-H, Chiang C-C, Yu N, Liu S-B (2011) Fabrication and electrocatalytic performance of highly stable and active platinum nanoparticles supported on nitrogen-doped ordered mesoporous carbons for oxygen reduction reaction. *J Chem Mater* 21:12489–12496
 41. Xiao H, Shao ZG, Zhang G, Gao Y, Lu WT, Yi BL (2013) Fe-N-carbon black for the oxygen reduction reaction in sulfuric acid. *Carbon* 57:443–451
 42. Liu S-H, Wu J-R (2011) Nitrogen-doped ordered mesoporous carbons as electrocatalysts for methanol-tolerant oxygen reduction in acid solution. *Int J Hydrogen Energy* 36:87–93
 43. Wu HM, Wexler D, Liu HK (2011) Durability investigation of graphene-supported Pt nanocatalysts for PEM fuel cells. *J Solid State Electrochem* 15(5):1057–1062
 44. Selvaganesh SV, Sridhar P, Pitchumani S, Shukla AK (2014) Pristine and graphitized-MWCNTs as durable cathode-catalyst supports for PEFCs. *J Solid State Electrochem* 18(5):1291–1305